ADVANCED SUSTAINABLE SYSTEMS
www.advsustainsys.com

Oleo-Dispersions of Electrospun Cellulose Acetate Butyrate Nanostructures: Toward Renewable Semisolid Lubricants

Manuel A. Martín-Alfonso, José F. Rubio-Valle, José E. Martín-Alfonso, and José M. Franco**

In this work, the electrospinnability of cellulose acetate butyrate (CAb) solutions, and the ability of the resulting micro- and nano-architectures to structure castor oil are studied aiming to develop eco-friendly lubricating greases. Particles, beaded-fibers, defect-free fibers, and porous nanostructures are successfully prepared by dissolving CAb in *N,N*-dimethylacetamide/acetone (DMAc:Ac, 1:2 w/w) and methylene chloride/acetone (DM:Ac, 1:1 w/w) solvent mixtures at different concentrations (2.5–15 wt.%). The formation of bead-free nanofibers is favored at concentration above 10 wt.%, when solutions achieve relaxation times of ≈50 ms and shear-thinning in extensional and shear flow tests, respectively. Non-porous and porous CAb nanostructures are successfully used as castor oil thickeners at concentrations of 3–5 wt.%, leading a wide variety of rheological responses which mimic those of traditional semisolid lubricants. The surface properties of the nanofibers have a significant impact on the wear and friction performance in metal–metal contact, which has been associated with the oil release ability of the generated 3D network. Oleo-dispersions prepared with smooth fibers show tribological performance comparable to, or even better than, commercial lithium greases. Overall, this study reveals the potential of CAb electrospun nanostructures for the development of next-generation renewable semisolid lubricant formulations.

1. Introduction

The transition to a circular economy entails system-level innovations that design out waste, maximize resource value and minimize negative environmental impacts, which is a challenge for both industry and the academia. One important process or technology, where renewability and biodegradability must be taken into account, is lubrication aiming to reduce and control the friction and wear. Lubrication has a vital position in terms of efficiency and reliability of numerous mechanical devices, industrial equipment, transportation hardware, etc..., with examples including pumps, gears, vehicles, trains, aircraft, and so on.[1,2] It has been estimated that ≈30% of the world's primary energy resources are consumed by friction and ≈80% of the mechanical components of machinery fail because of wear.[3] Therefore, improvements in lubrication by developing advanced lubricants could save annually billion US dollars worldwide while also reducing CO_2 emissions by million tons per year, with an accompanying vast decrease in PM2.5 emissions.[4] In addition to the technical efficiency, in the last years, as a result of government regulations, or due to the increasing public concern for a pollution-free environment, the environmental impact of lubricants has taken on a key role. It has been predicted that ≈50% of produced lubricant volume ends up in the environment every year.[5,6]

Semisolid lubricants are multicomponent formulations that typically include or are processed using toxic substances, such as polycyclic aromatic hydrocarbons, zinc dialkyl dithiophosphate, tri-o-cresyl phosphate, or metallic soaps, among others.[7–9] The usual approach to reduce the environmental impact and improve the renewability or biodegradability of lubricating fluids and greases involve the use of vegetable oil-derived base oils. However, other ingredients required to improve the rheological and tribological properties or just to thicken the lubricant oil to form a semisolid lubricant must also meet the sustainability criteria. Aiming to achieve fully green lubricating greases, the utilization of thickeners derived from renewable materials such as biopolymers or nanoclays with less or no harmful components has been addressed.[10–13] Among the portfolio of renewable materials available today, many biopolymers such as chitin, chitosan, lignin, cellulose, and their derivatives have been used as raw materials to prepare thickener agents.[14–17] Nevertheless, some limitations concerning the compatibility with the base

M. A. Martín-Alfonso, J. F. Rubio-Valle, J. E. Martín-Alfonso, J. M. Franco
Chemical Product and Process Technology Research Center (Pro^{2}TecS)
Department of Chemical Engineering and Materials Science
ETSI
University of Huelva
Huelva 21071, Spain
E-mail: jose.martin@diq.uhu.es; franco@uhu.es

The ORCID identification number(s) for the author(s) of this article can be found under https://doi.org/10.1002/adsu.202300592

DOI: 10.1002/adsu.202300592

oil, the physical stability, the temperature resistance, or the need to chemically modify these biopolymers to improve these drawbacks have not yet been fully addressed. Some authors[17–19] pointed out that native cellulose, i.e., non-chemically modified, can be effectively used as thickener in lubricating greases in the form of nanoparticles or microfibrils and emphasized the role of the base oil to provide stability of thickener particles against aggregation and sedimentation. Thus, for non-modified cellulose, polar base oils such as triethyl citrate or di(2-ethylhexyl) sebacate are preferred. Moreover, the addition of clays can create a percolation network with suitable rheological characteristics to prevent aggregation and sedimentation of the cellulose particles.[18] Very recently, a novel strategy consisting of the development of electrospun nanostructures as an alternative approach for structuring vegetable oils has been reported.[20–22] Nanofiber-based architectures conveniently dispersed, due to the combination of their small size and high surface/volume ratio, promote oil structuring. Thus, the development of oleo-dispersions based on electrospun biopolymer nanostructures is a hot topic to address the environmental problems of lubricants.

Among green polymers, cellulose acetate and its derivatives such as cellulose acetate butyrate (CAb) are attracting considerable attention. For instance, CAb gels in acetyl tributyl citrate have been recently investigated as low-temperature greases.[23] CAb is one of the toughest of the cellulose acetate derivatives, and presents good mechanical properties, transparency, colourability, and resistance to inorganic chemicals.[24–26] CAb has a relatively hydrophobic character owing to the presence of acetyl and butyryl groups in the glucose unit, allowing its dissolution in organic solvents. Thus, the electrospinnability of CAb has been addressed in a few previous works.[27–31] Huang et al. discussed the formation mechanism of a parallel line surface on electrospun CAb fibers using a solvent mixture of acetone and *N,N*-dimethylacetamide, which was attributed to the formation of voids on the jet surface at the early stage of electrospinning and subsequent elongation and solidification of the voids into a line surface structure.[31] Tanvir et al. created porous CAb nanofibers using electrospinning in high humidity conditions to explore their potential as oil sorbents.[28] Hosseini et al. prepared CAb nanofibers, and described the potential use of fibers to separate the contaminants from an industrial tomato wastewater.[30] In addition, hybrid nanocomposites based on CAb were prepared using electrospinning. Pascariu et al. described a new procedure for synthesis of hybrid CAb–ZnO electrospun nanocomposites and tested as photocatalysts for dye degradation.[29] While, Tan et al. discussed the development of CAb and polyethylene glycol (PEG) electrospun composite scaffolds as a biomaterial for tissue engineering applications.[27] Nevertheless, up to date a systematic study on the correlation between the electrospinnability of CAb solutions, considering their physicochemical and rheological properties, and the capacity of the nanoarchitectures generated to structure vegetable oils has not been undertaken.

Aiming to overcome this gap, the objective of this work was to develop oleo-dispersions based on electrospun CAb nanostructures and castor oil that could be potentially implemented as sustainable semisolid lubricant formulations. The final target is that these renewable compositions can provide similar or better rheological characteristics and tribological performance than multipurpose lithium lubricating greases. To achieve this goal, the influence of physicochemical and shear and extensional rheological properties of CAb solutions on its electrospinnability was studied. A spectrum of nanoarchitectures, including porous structures, susceptible for structuring vegetable oils was obtained by tuning the solution properties. Then, the impact of nanostructure morphology, surface properties and concentration on the rheological, tribological and functional properties of the resulting oleo-dispersions was comprehensively assessed.

2. Results and Discussion

2.1. Physico-Chemical Properties of CAb Solutions

Some physico-chemical properties of CAb solutions in the *N,N*-dimethylacetamide/acetone (DMAc:Ac) binary solvent such as surface tension, electrical conductivity and shear and extensional viscosities were studied and analyzed attending their direct relationship with the electrospinning process.[32–36] The values of these physical properties as function of CAb concentration are shown in **Table 1**. As can be observed, the values of surface tension decrease with CAb concentration from 23.3 to 15.4 mN m^{-1}. This reduction facilitates the electrospinning process by counteracting the electrical forces, and helps to form a continuous fluid jet from the syringe tip.[32,37] Similar change in surface tension values with polymer concentration was for instance observed PEO and PVA solutions in water.[38] The evolution of the electrical conductivity was different. First, the values of electrical conductivity increase up to 2.52 μS cm^{-1} for a CAb concentration of 10 wt.% and then decrease. In principle, the initial increase of electrical conductivity suggests that the solutions are below the entanglement concentration, i.e., in the semidiluted unentangled regime, whereas above a critical concentration the reduced mobility of the entangled macromolecules causes the conductivity to decrease. Similar evolution of the conductivity with polymer concentration have been reported previously for other biopolymers.[20,22]

Figure 1a displays the log–log plot of the viscosity versus shear rate for CAb solutions at concentrations ranging from 1.5% to 20 wt.%. All the solutions showed a Newtonian behavior for concentrations lower than 7.5 wt.%, with viscosity values ranging between 0.009 and 0.169 Pa s. However, at higher polymer concentrations the flow behavior turned to shear thinning above a critical shear rate (see Figure 1a). As can be observed, this flow behavior is characterized by three different regions: i) a Newtonian region at low shear rates (η_0); ii) a shear thinning region follows at intermediate shear rates; and iii) a tendency to reach a constant high-shear rate limiting viscosity (η_∞).[39] This shear rate dependence of viscosity fitted fairly well the Carreau-Yasuda model (Equation (3)). The values of the Carreau–Yasuda model fitting parameters are shown in Table 1. The zero- and high-shear rate limiting viscosities (η_0 and η_∞) increased with CAb concentration, as a consequence of the thickening effect in the bulk phase. Regarding the shear thinning region, the critical shear rate ($\dot{\gamma}_c$) for the onset of the non-Newtonian region slightly decreases with CAb concentration, while the characteristic slope of viscosity related with *p* and *s* dimensionless values increases with concentration.

When plotting the specific viscosity, η_{sp} (being $\eta_{sp} = (\eta/\eta_s)-1$, where η_s is the solvent viscosity), as a function of CAb concentra-

Table 1. Surface tension, electrical conductivity, shear viscosity (η), extensional viscosity (η_{ext}) and relaxation time (λ_E) values and Carreau–Yasuda fitting parameters for CAb spinning solutions in 1:2 DMAc:Ac.

Spinning solutions	Surface tensión, σ [mN m^{-1}]	Electrical conductivity, Λ [μS cm^{-1}]	Newtonian viscosity, η [Pa s]	η_0 [Pa s]	η_∞ [Pa s]	$\dot{\gamma}_c$ [1/s]	p [–]	n [–]	Extensional viscosity, η_{ext} [Pa s]	Relaxation time, λ_E [ms]
CAb-free solvent	25.6	1.09	0.0007							
1.5 wt.% CAb	23.3	1.57	0.0085	–	–	–	–		0.03	–
2.5 wt.% CAb	23.1	1.65	0.011	–	–	–	–		0.03	–
3 wt.% CAb	22.9	1.71	0.016	–	–	–	–		0.05	–
4 wt.% CAb	22.6	1.83	0.029	–	–	–	–		0.08	–
5 wt.% CAb	22.5	2.01	0.056	–	–	–	–		0.17	5
7.5 wt.% CAb	22.2	2.29	0.169	–	–	–	–		0.49	19
10 wt.% CAb	20.9	2.52	–	0.58	0.11	21.4	2.24	0.09	8.09	51
15 wt.% CAb	18.6	2.30	–	7.50	0.48	8.88	2.86	0.04	25.72	349
20 wt.% CAb	15.4	2.04	–	20.6	0.63	7.65	1.90	0.02	63.22	–

tion in log-log scales (Figure 1b), the transition from the semidilute unentangled regime to the semidilute entangled regime can be detected by a change in slope. This change in slope occurs at the so-called entanglement concentration, C_e. From Figure 1b, it can be easily deduced that C_e in the DMAc:Ac binary solvent is ≈4.7 wt.%, which is one decade higher than the overlap concentration ($C_e \approx 10C^*$) that delimits the dilute and semidilute regimes in polymer solutions,[40,41] where C^* is assumed to be $0.77/[\eta]$, i.e., 0.46 wt.%, according to Graessley.[42] Below C_e, $\eta_{sp} \approx C^{1.3}$, which is in agreement with the scaling exponent predicted by the Rouse model for neutral polymers in good solvents in the semidilute unentangled regime, whilst $\eta_{sp} \approx C^{4.1}$ for the entangled regime, which is also the predicted ≈×3 larger scaling exponent values above C_e.[40,41] C_e can be used to roughly predict the adequate electrospinnability of polymer solutions and the morphology of electrospun structures.[43,44] Thus, it has been proposed that the solution concentration should be at least 2–2.5 times C_e.[43,44] Different fiber morphologies, such as beaded-fibers and uniform free bead-fibers, have been associated with different polymer concentration domains.[40] As discussed below, CAb solutions with concentrations higher than 10 wt.% are more likely to be suitable for obtaining uniform bead-free fibers. Figure 1b also compares the specific viscosity values of CAb in the 1:1 (wt./wt.) dichloromethane/acetone (DM:Ac) binary solvent. As can be seen, CAb behaves hydrodynamically very similar in both binary solvents, being C_e approximately 4.2 wt.% in 1:1 (wt./wt.) DM:Ac.

Extensional flow properties of CAb solutions were obtained from the time evolution of the fluid filament diameter. Figure 1c shows the results of the normalized filament diameter evolution as a function of CAb concentration. As can be seen, initially an inertial capillary-driven flow regime characterized by a decay of the diameter with a power-law behavior[45] is observed, typically found in low viscous fluids where the capillary pressure is only resisted by the inertia of the accelerating fluid molecules.[46] However, for CAb concentrations >10 wt.%, an additional elastic component is apparent during the filament-thinning process, characterized by an exponential decay of the diameter with time.[37,47] Also, it can be observed that the filament break-up time increased with increasing CAb concentration. Moreover, in the terminal regime of the filament-thinning process, the normalized diameter decreases faster than expected from a single exponential decay, resulting in a downward curvature of the curves. According to this, the characteristic relaxation time, λ_E, can be estimated by fitting these filament-thinning profiles to the following equation:[48]

$$\frac{D(t)}{D_0} = Ae^{-Bt} - Ct + D \quad (1)$$

where A, B, C, and D are fitting parameters. Parameter B is directly related to the extensional relaxation time as follows: $B = 1/3\lambda_E$.[49] Table 1 collects the values of relaxation time, λ_E, as a function of the CAb concentration. An important increase in the relaxation time for CAb concentrations higher than 10 wt.% can be observed. This behavior is clearly a manifestation of the enhanced interactions between CAb molecules in solution beyond this critical concentration, which is also evidenced by the increasing values of the extensional viscosity (Table 1). For concentrations <5%, the relaxation time was neglected since A values are extremely low. Similar extensional behavior has been shown in several studies for solutions of cellulosic and gum derivatives.[45,50]

2.2. Electrospinnability of Cellulose Acetate Butyrate

Figure 2 displays the morphology of electrospun nanostructures as a function of CAb concentration and binary solvent system used to prepare the spinning solutions. As shown in Figure 1b, the influence of CAb concentration on the specific viscosity was similar for both binary solvent systems (DMAc:Ac and DM:Ac) studied and, therefore, the expected critical concentration to be adequately electrospun as well. For low concentrations (2.5–5 wt.%) a continuous jet in the electrospinning process was obtained. However, the obtained electrospun mats were largely irregular, comprising non-uniform microparticles and hairy-beaded structures, respectively. The average particle size increased from ≈860 nm to ≈2.5 μm when DMAc was replaced by DM in the binary solvent system and, more importantly, irregular pores were extensively observed on the microparticles. This is a clear indication of low viscosity (i.e., low level of entanglements) of these solutions, and thus the concentration was increased to investigate the changes in morphology. For

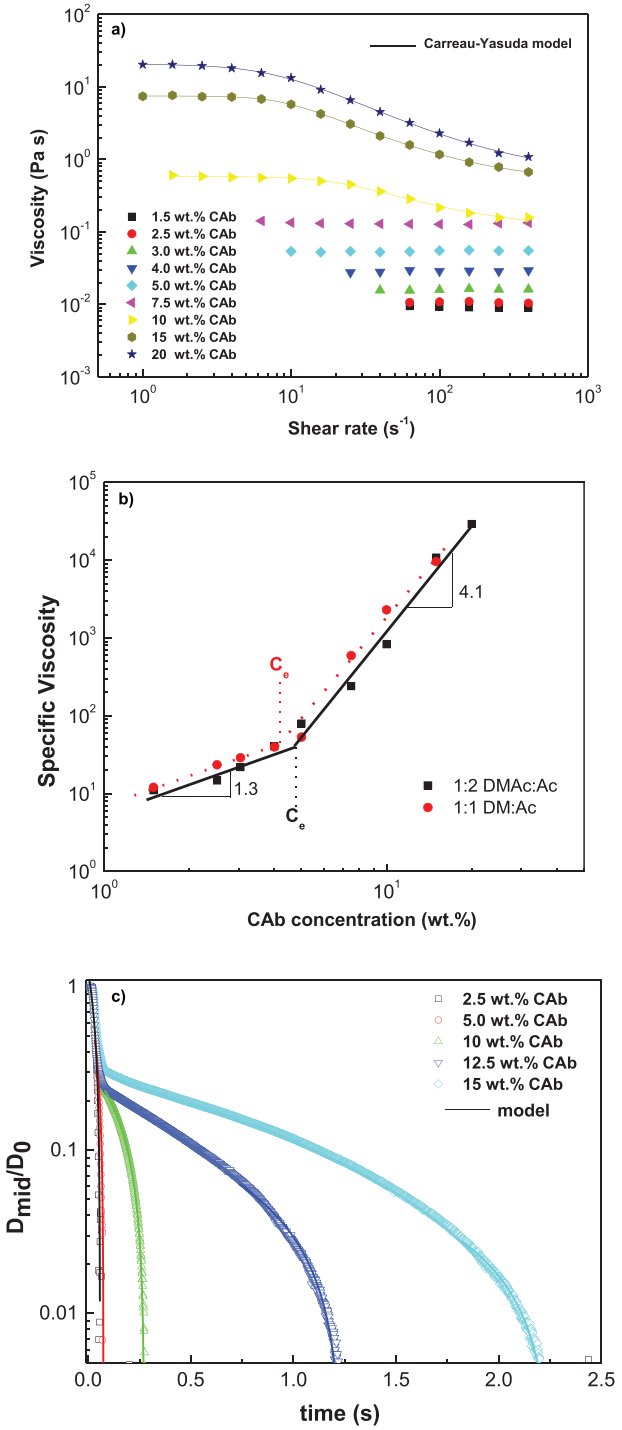

Figure 1. a) Viscous flow curves, b) specific viscosity versus concentration plot, and c) normalized filament diameter versus time plots in extensional measurements, for CAb solutions in 1:2 DMAc:Ac. For the sake of comparison, specific viscosity data for CAb solutions in 1:1 DM:Ac have also been included in inset (b).

7.5–10 wt.% concentrations, bead-on-string (BOAS) morphologies were observed, along with irregular pores on the surface of beads and fibers for solutions formulated with DM:Ac. The average pore diameter was found to be in the range of 45–110 nm. The formation of nanopores can be explained according to the rapid evaporation of a highly volatile solvent (DM). It results in a large amount of heat being absorbed as it evaporates thereby cooling the surface of the fibers. This cooling effect causes water vapour from the humid environment to condense as droplets on the fibers surface and, upon drying, the water droplets evaporate leaving behind pores.[51] Finally, at CAb concentration higher than 10 wt.%, uniform fibers were observed, with an average fiber diameter of 581 nm for the DMAc:Ac solutions. However, SEM images showed that CAb fibers produced with DM:Ac binary solvent had a ribbon-like morphology (Figure 2j). The formation of ribbon-like morphologies is again due to rapid vaporization of DM from the surface of the jet and hence collapsing the resulted fibers. When the jet is collapsed, the diametrically opposite parts of the fiber skin come into contact and small tubes are formed at each edge of the ribbon.[52] On the basis of these results, it is worth saying that the electrospinning process was more unstable for solutions prepared with DM:Ac, which is mainly interrupted by nozzle clogging. It is well known that the shape and size of electrospun nanostructures are directly affect by the solution parameters such as viscosity, surface tension and electrical conductivity. As has been mentioned previously, the viscosity and conductivity increase and the surface tension decreases as the solution concentration increases. All the three parameters favor the formation of smooth fibers,[53] when the concentration increases to ≈10 wt.%. According to Figure 1b, solutions in the semidilute non-entangled regime produced irregular and non-uniform microparticles, solutions at concentrations slightly above C_e in the semidilute entangled regime produced hairy-beaded structures and BOAS morphologies, while CAb concentrations above 10 wt.% (≈2–2.5 times C_e) yielded uniform fibers.

According to these results and considering that surface tension in CAb solutions is approximately constant at the concentrations studied, the rheological properties under shear and elongation are the major determining factors on fiber morphology under similar electrospinning conditions. A critical point exists, which lies ≈10 wt.%, above which molecular entanglements are sufficient[54] to produce defect-free fibers instead of BOAS morphologies. Further, an extensional flow transition from a visco-capillary balance to an elasto-capillary balance was observed about this concentration, at a threshold value (≈50 ms) of the characteristic relaxation time. These results are in agreement with the observations obtained by Yu et al.[55] related to the fact that solution elasticity, as measured by relaxation time, is an essential property controlling the morphology of the fibers produced by electrospinning. It is worth noting that the trend of the relaxation time is in good agreement with the electrospinnability of polymer in term of fiber diameter size, as can be observed in **Figure 3a**. Indeed, higher CAb concentrations cause an increase in both relaxation time and fiber diameter (see Figure 3b).

2.3. Rheology, Tackiness, and Oil Loss of CAb Oleo-Dispersions

Figure 4a–c depicts the mechanical spectra of CAb oleo-dispersions as a function of spinning solution concentration

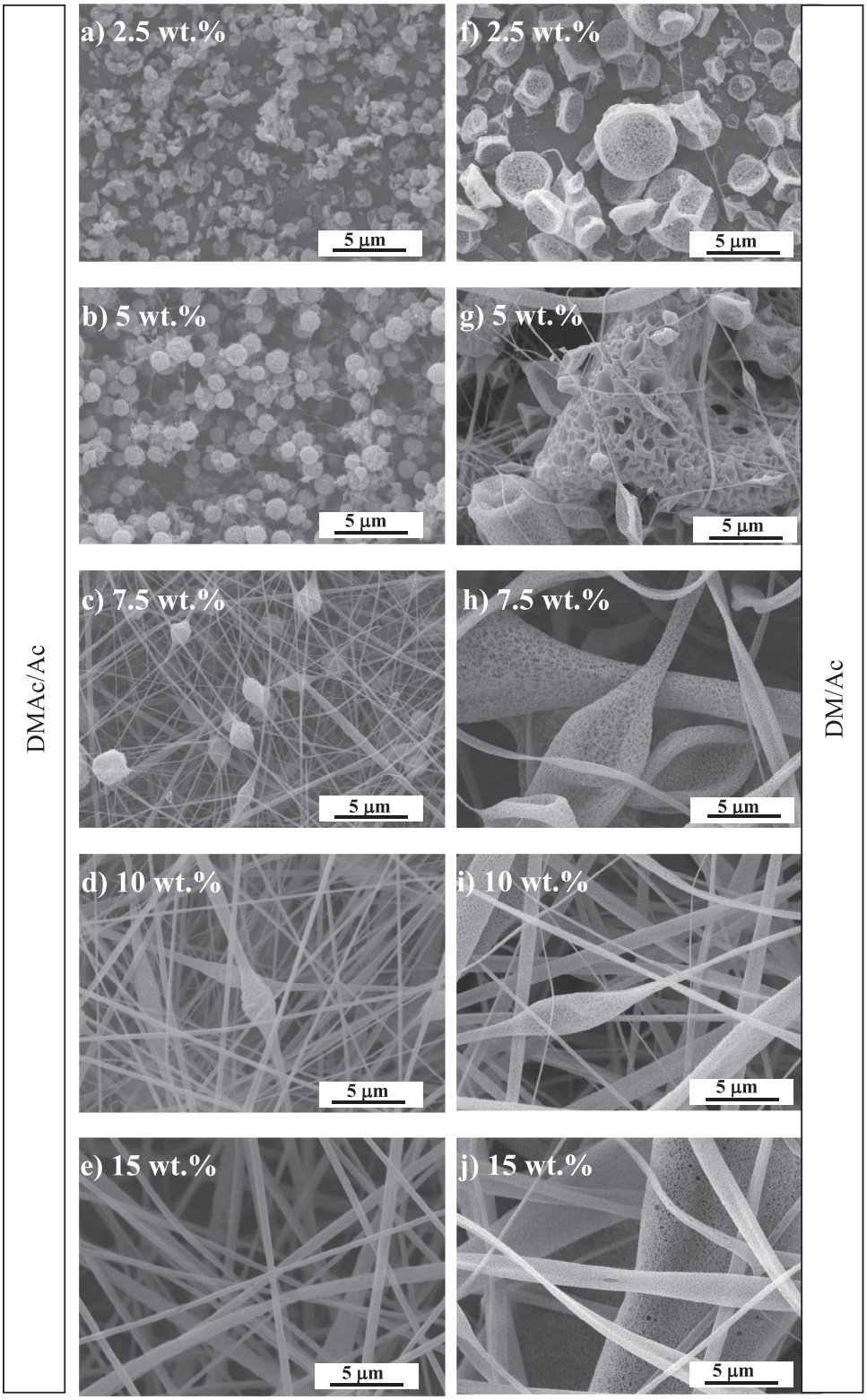

Figure 2. Representative SEM images of electrospun nanostructures obtained from CAb solutions in both 1:2 DMAc:Ac: a) 2.5 wt.%, b) 5 wt.%, c) 7.5 wt.%, d) 10 wt.%, e) 15 wt.%, and 1:1 DM:Ac: f) 2.5 wt.%, g) 5 wt.%, h) 7.5 wt.%, i) 10 wt.%, j) 15 wt.% respectively.

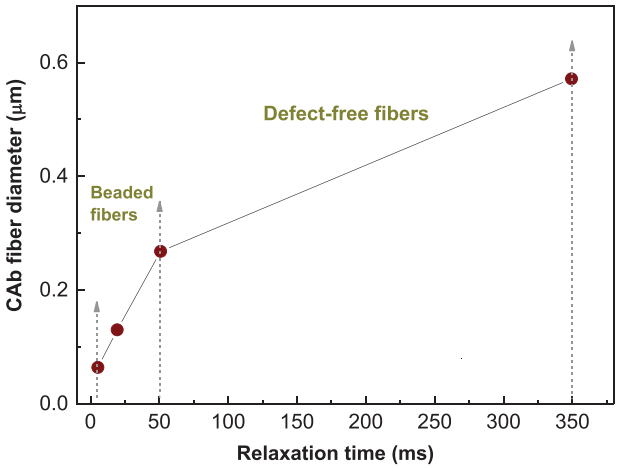

Figure 3. Average diameter of electrospun fibers versus relaxation time of CAb solutions.

(in the DMAc:Ac binary solvent) and nanostructure content for both smooth and porous fibers, respectively. As shown in Figure 4a, a drastic change in the evolution of the storage (G′) and loss (G″) moduli with the angular frequency was clearly observed when CAb concentration in the spinning solution was increased from 2.5 to 5 wt.%, for the same thickener concentration. For the lowest concentration (2.5 wt.%), a liquid-like response was detected where the viscous component (G″) predominated over a wide frequency range. at low frequencies, whereas the elastic response prevailed at high frequencies, so there was a crossover in the two moduli at high frequencies. However, for CAb solution concentrations between 5 and 15 wt.%, G′ > G″ over the entire frequency range, G′ slightly increases with frequency and G″ displays a minimum, which is known as the "plateau" region of the mechanical spectrum, suggesting a gel-like behavior.[56] This region is characteristic of the occurrence of physical entanglements in polymeric materials[57] In this case, it may be attributed to the packing effect of the percolation network formed among electrospun fibers. Despite the mechanical spectrum pattern was preserved, the higher the spinning solution concentration, the higher the values of both viscoelastic moduli of resulting oleo-dispersions for a 5 wt.% nanostructure content.

Figure 4b displays the influence of thickener (i.e., the electrospun nanostructures) concentration on the mechanical spectra of dispersions obtained with CAb smooth nanofibers obtained from a 15 wt.% spinning solution in a DMAc:Ac binary solvent system. As can be observed, all oleo-dispersions exhibited a similar gel-like behavior, which is also very similar to that shown by the standard lithium grease taken as benchmark. As expected, increasing the thickener concentration resulted in higher values of both G′ and G″, although not significantly affecting the relative elasticity, i.e., the loss tangent (G″/G′), which indicates that the basic fiber-oil interaction was not altered but only the progressive increase in the number of transient junction zones of fibers due to packing effects. It is remarkable that the mechanical spectrum of the lithium grease was reasonably mimicked by the oleo-dispersion containing 5 wt.% nanofibers, being the lithium soap content of typical NLGI 1–2 grade greases in the range of 10–18 wt.%. A similar behavior was found for oleo-dispersions formulated with porous nanofibers obtained by electrospinning of CAb solutions in the 1:1 DM:Ac binary solvent (Figure 4c). However, the values of viscoelastic moduli were higher than those obtained with smooth nanofibers as well as the relative elasticity, i.e., lower values of the loss tangent. The values of the "plateau" modulus, G^0_N, which is a characteristic parameter for the plateau region defined as the extrapolation of the contribution of the level of entanglements to G′ at high frequencies,[58] was plotted in Figure 4d, for both types of nanofibers. For example, at 4 wt.% nanofiber concentration, the use of porous nanofibers instead of smooth ones made G^0_N to increase from 10 240 to 28 800 Pa, i.e., a 2.8-fold increment.

Table 2. Unworked penetration values, NLGI grades and dropping points of the oleo-dispersions prepared with 5 wt.% smooth and porous fibers (obtained with the DMAc:Ac and DM:Ac binary solvents, respectively, and 15 wt.% spinning solution concentration) in comparison with those shown by the commercial lithium lubricating grease taken as reference systems.

Oleo-dispersions	Penetration [dmm]	NLGI grade	Dropping point [°C]
Smooth fibers (5 wt.%)	265±9	2	165
Porous fibers (5 wt.%)	267±11	2	155
Lithium grease	301±19	1-2	190

For the sake of comparison, the unworked penetration values, together with the corresponding NLGI grades, and dropping points of the oleo-dispersions containing 5 wt.% nanofibers, which reasonably mimic the SAOS functions of the lithium grease, are shown in **Table 2**. As can be seen, despite the very similar values of the SAOS functions, the oleo-dispersions containing 5 wt.% nanofibers have slightly higher consistency, i.e., lower penetration values, than the lithium grease with presumably much higher thickener content. However, the dropping points are lower.

Besides SAOS measurements, tackiness tests were performed to evaluate the cohesiveness and stickiness of these oleo-dispersions, which are important properties in a lubricated contact. **Figure 5a–c** depicts the stress–strain curves of the oleo-dispersions obtained from tack experiments as a function of the spinning solution concentration and thickener content of smooth and porous fibers. The stress–strain profiles are typical for slow debonding velocities caused by cohesive samples between two parallel plates. The separation is initially characterized by the extensional flow of the fluid where the force rises to a maximum that represents the work required to separates the plates and then the force decreases to zero, corresponding with the work required to break the filaments and/or debond the sample from the surfaces. The area under this second part of the curve gives access to the tackiness energy per unit area (E_{tac}) which can be calculated as follows:[59]

$$E_{tac} = h_0 \int_{\varepsilon_{max}}^{\varepsilon_{final}} \sigma(\epsilon)\, d\epsilon \quad (2)$$

where σ is the normal stress and ϵ is the elongational strain.

As can be observed in Figure 5a–c, according to the maximum peak stress and area reached during the test, the tackiness of the

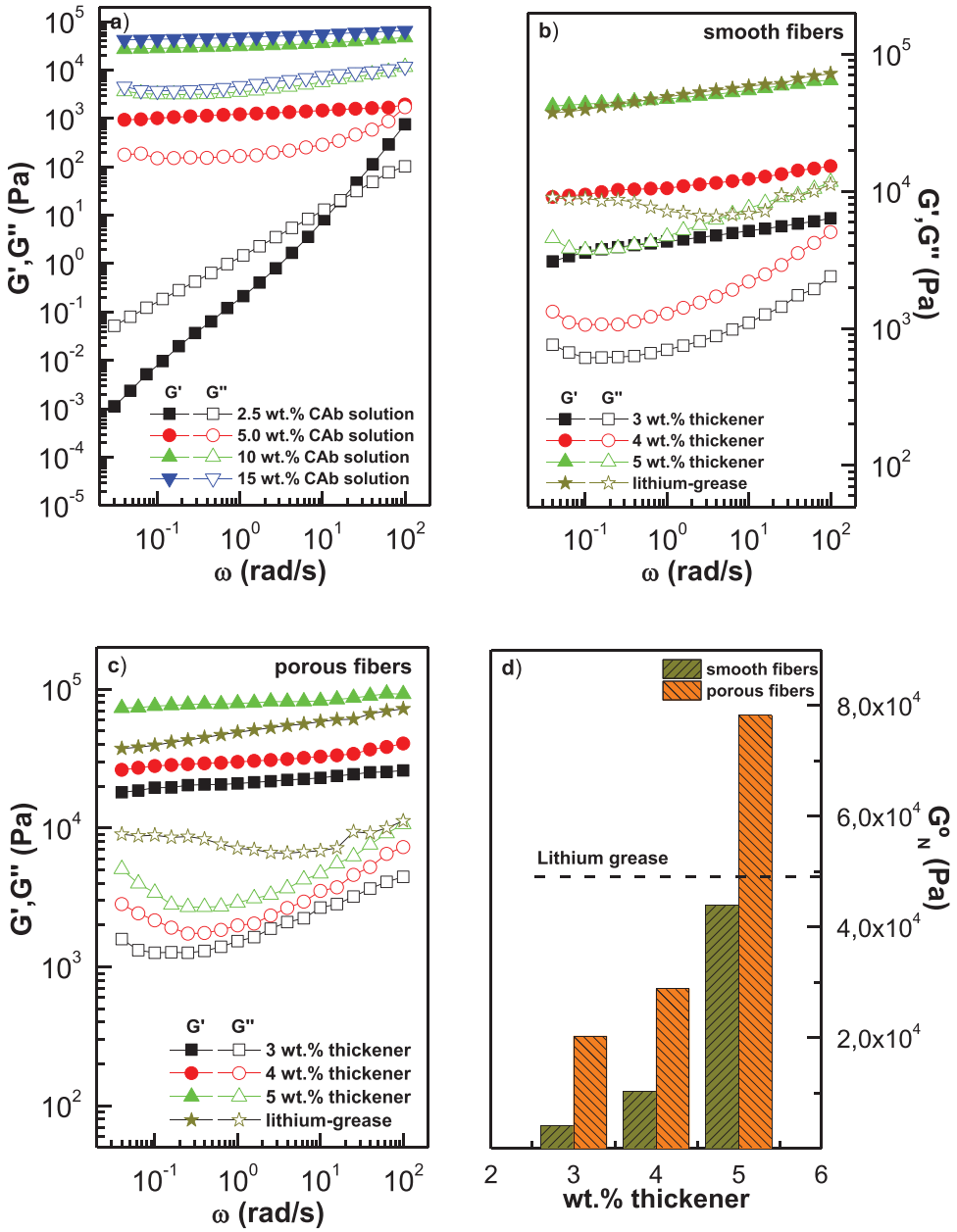

Figure 4. Mechanical spectra of oleo-dispersions as a function of a) concentration in the DMAc:Ac spinning solution (5 wt.% thickener concentration), b) thickener content for smooth fibers (obtained with 15 wt.% spinning solution concentration in DMAc:Ac) and c) thickener content for porous fibers ((obtained with 15 wt.% spinning solution concentration in DM:Ac); and d) evolution of the plateau modulus ($G°_N$) with thickener content for oleo-dispersions prepared with smooth and porous fibers. Data obtained with a commercial lithium lubricating grease have been included for reference.

oleo-dispersions studied increased with both the spinning solution concentration (data shown for the DMAc:Ac binary solvent) and the thickener content. Interestingly, the tackiness found for oleo-dispersions formulated with CAb porous nanofibers (Figure 5c) was much lower than that obtained with smooth nanofibers. This is explicitly reflected in the values of tackiness energy (see Figure 5d). Obviously, the entanglement network of the oleo-dispersions, which is determined by the nanostructure morphology and amount of thickener, plays a key role in controlling the extensional deformation of the network and tackiness observed. In this sense, the tackiness decreases when both the number of particles or beads and porosity in nano-architectures generated by electrospinning increase, while increases with the density of entanglements. This can be explained taking into account that the oleo-dispersions formulated with BOAS-based nanostructures and with a lower concentration of thickener present a lower density of fibers and/or thinner fibers, and therefore the gel networks need lower forces to debond the contact. In addition, oleo-dispersions formulated with these morphologies generally showed a lower gel-strength or even a liquid-like

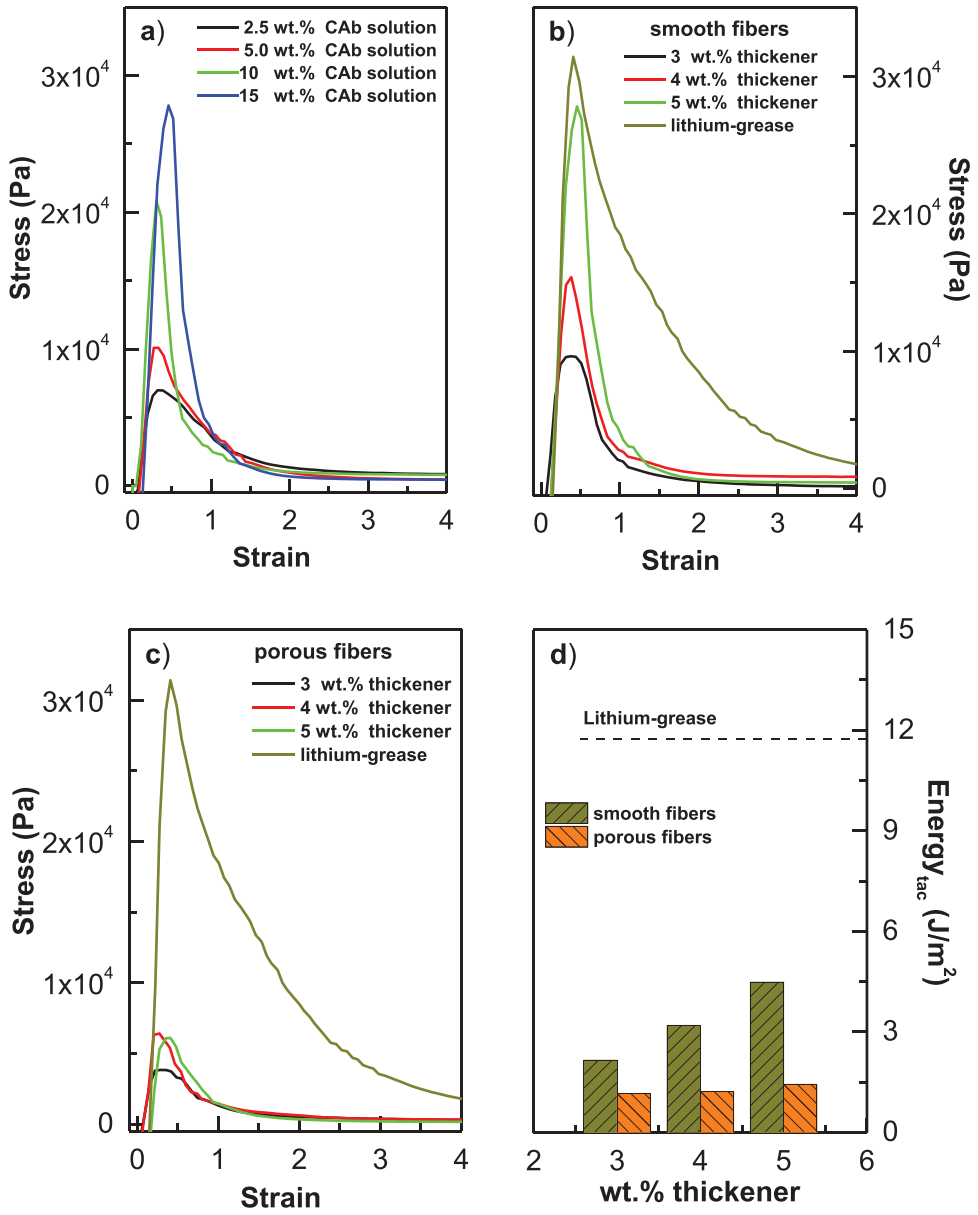

Figure 5. Stress–strain plots in tacking tests as a function of a) CAb concentration in the DMAc:Ac spinning solution (5 wt.% thickener concentration), b) thickener content for smooth fibers (obtained with 15 wt.% spinning solution concentration in DMAc:Ac) and c) thickener content for porous fibers (obtained with 15 wt.% spinning solution concentration in DM:Ac); and d) change of tackiness energy (E_{tac}) with thickener content for oleo-dispersions prepared with smooth and porous fibers. Data obtained with a commercial lithium lubricating grease have been included for reference.

response, causing a reduction in tackiness,[59] which have been previously corroborated by means of SAOS tests. However, the low tackiness of oleo-dispersions prepared with the porous nanostructures cannot be linked with this fact. We hypothesize that the oil can penetrate into the porous nanostructures and be adsorbed not only on the external surface but also on the inside, enhancing the oil-thickener interaction, which would result in a higher gel strength, as shown in SAOS tests. However, these porous nanostructures give rise to a less cohesive network and are less resistant to extensional deformations, leading to a decrease in tackiness, which may be associated to both a higher nanofiber weakness and a lower free oil level available.

To corroborate this hypothesis, oil loss measurements were performed as indicator of the oil-binding capacity of the different nanostructures. **Figure** 6a,b displays the oil loss (%) in oleo-dispersions prepared with smooth and porous fibers, respectively. All the oleo-dispersions presented self-supporting gel-like networks, but oil loss decreases with thickener concentration as the fiber density in the percolation network increases, associated to packing effects. Further, the amount of oil loss was reduced when porous fibers were used, which is concordance with the presumed higher functional surface ratio. Moreover, the oleo-dispersions formulated with smooth CAb nanofibers (Figure 6c) evidence signs of lubricant oil at the periphery as

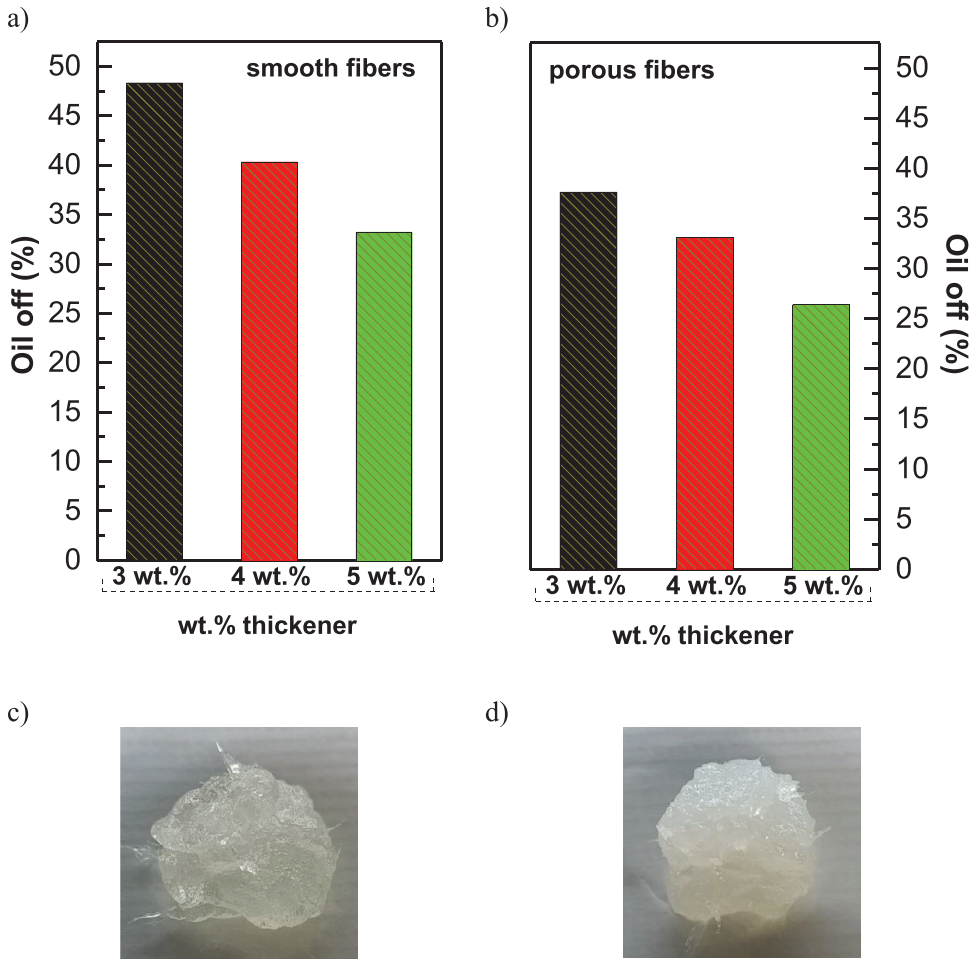

Figure 6. a,b) Oil loss after centrifugation and c,d) visual appearance for oleo-dispersions containing different concentration of smooth fibers (a and c, respectively) and porous fibers (b and d, respectively). Nanofibers obtained from 10 wt.% CAb concentration in the spinning solution.

may be noticed by the brightness in the images, while the oleo-dispersions formulated with CAb porous fibers show a "dryer" appearance (Figure 6d). In any case, all the nanostructures present a good oil-binding capacity and are physically stable against phase separation. By contrast, dispersions of non-electrospun CAb in castor oil separate immediately, and only a small amount of oil is retained (≈15% wt.) due to a certain swelling. These results confirm that porous nanostructures have higher efficiency in enhancing the oil-thickener interaction.

2.4. . Lubrication Properties of CAb Oleo-Dispersions

The lubrication performance of the oleo-dispersions was tested in a steel–steel ball-on-plates sliding contact by applying rotational speed sweeps. **Figure 7** displays the friction coefficient versus sliding velocity plots for a 40N normal load (Hertzian pressure of 1.29 GPa) and oleo-dispersions formulated with different concentrations of smooth fibers obtained with the DMAc:Ac binary solvent (3–5 wt.%). The mixed and hydrodynamic lubrication regimes can be recognized. At very low sliding velocities, presumably nearby the boundary lubrication regime, the normal force is supported by the contacting asperities, and the friction is mainly determined by the solid contacts with negligible lubricant entrainment into the contact area. As the sliding velocity increases, in the mixed lubrication regime, the fluid inlet in the contact zone is enough to partially separate the ball from the plates, being the lubricant film thickness and length of the surface asperities of similar sizes. This implies that, in the mixed regime, both bulk lubricant rheology and surface properties have an influence on the friction which is significantly reduced. Finally, at high sliding velocities, a film of lubricant fully separates the surfaces and the friction coefficient increases with sliding velocity according to the bulk rheological properties of the lubricant. As can be observed in Figure 7, very similar evolution of the friction coefficient was observed for oleo-dispersion regardless the nanofiber content. In general, a reduction in the friction coefficient in the mixed/elastohydrodynamic lubrication regime was found as compared to the nanofiber-free castor oil. However, at high sliding velocities, the friction coefficient increases due to the transition from the mixed to the hydrodynamic lubrication regimes, which was not found with pure castor oil. This means that the transition from the mixed to the hydrodynamic lubrication regime was favored by the nanofibers. Interestingly,

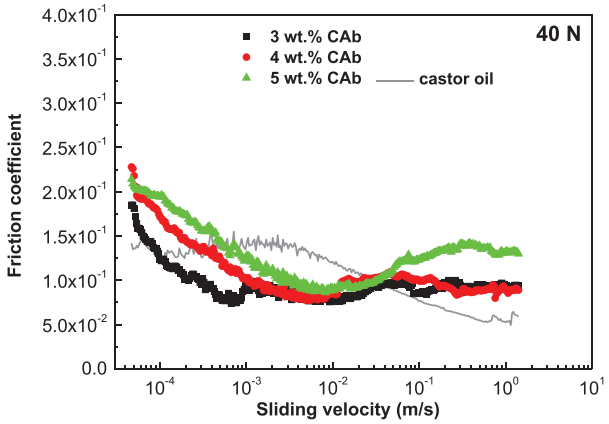

Figure 7. Friction coefficient versus sliding velocity curves using oleo-dispersions prepared with smooth fibers (obtained with the DMAc:Ac binary solvent and 15 wt.% spinning solution concentration) as lubricant, as a function of thickener concentration (applied normal load: 40 N).

the lowest friction coefficient values were attained under mixed lubrication for oleo-dispersions with 3 wt.% thickener, although the minimum value was very similar for all concentrations.

More substantively, **Figure 8** displays the friction coefficient versus sliding time curves for the oleo-dispersions of the smooth fibers obtained with the DMAc:Ac binary solvent, as a function of thickener content, for 0.047 m s^{-1} sliding speed and 40 N load. to evaluate the anti-wear properties. For the oleo-dispersions studied, the friction coefficient gradually decreases with the sliding time until reaching a practically constant value after ≈1000 s. On the contrary, the commercial lithium grease needed much shorter times to achieve constant friction values. This is probably due to a combination of two effects, the formation of the tribofilm which may be more time-dependent in the case of the oleo-dispersions,[60] and the modification of the rheological properties under high shear conditions. In any case, this evolution

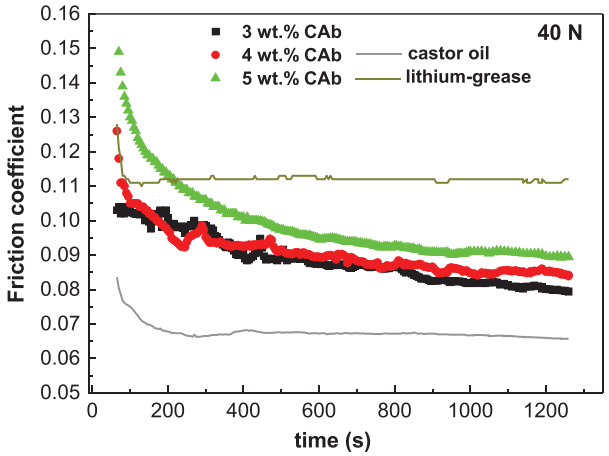

Figure 8. Evolution of the friction coefficient with time at constant sliding velocity (0.047 m s^{-1}) using the oleo-dispersions prepared with smooth fibers (obtained with the DMAc:Ac binary solvent and 15 wt.% spinning solution concentration) as lubricant, as a function of thickener concentration (applied normal load: 40 N). Castor oil and a commercial lithium lubricating grease are included for the sake of comparison.

Table 3. Friction coefficient values and average wear scar diameters obtained when using the oleo-dispersions prepared with smooth and porous fibers (obtained with the DMAc:Ac and DM:Ac binary solvents, respectively, and 15 wt.% spinning solution concentration) as lubricants. The commercial lithium lubricating grease and pure castor oil were included as reference systems.

Oleo-dispersions		Friction coefficient [–]	Wear scar diameter [μm]
Smooth fibers	3 wt.% thickener	0.080 ± 0.013	375 ± 15
	4 wt.% thickener	0.085 ± 0.012	318 ± 14
	5 wt.% thickener	0.089 ± 0.014	305 ± 17
Porous fibers	3 wt.% thickener	0.108 ± 0.011	664 ± 18
	4 wt.% thickener	0.112 ± 0.014	655 ± 16
	5 wt.% thickener	0.119 ± 0.016	652 ± 13
Castor oil (CAb-free)		0.068 ± 0.005	531±13[a]
Lithium grease		0.111 ± 0.017	521±19

[a] Data taken from Delgado et al.[65]

of the friction coefficient confirms the formation of the in situ protective film,[61] finally yielding lower friction coefficient values than those achieved with the lithium grease. As can be observed in **Table 3**, the friction coefficient values increase with thickener concentration, presumably associated with the lower oil release ability (see Figure 6) and/or penetration of a higher fiber content into the contact. Thus, the oil bleeding ability by action of an external force favours the lubricant replenishment of the contact.[62,63] Moreover, the penetration of fibers into the contact in the mixed lubrication regime significantly contribute to friction,[20,64] as can be deduced from the comparison of the friction coefficient values obtained with the oleo-dispersions and the CAb-free castor oil (see Figure 8 and Table 3). Considering the morphology of the nanostructure used to structure the oil, as shown in Table 3, lower friction coefficient values were obtained for oleo-dispersions formulated with porous nanostructures, more prone to retain oil (see Figure 6), which however are very similar to the value obtained with the lithium grease.

Figure 9 shows wear scar SEM micrographs of the worn surfaces of the steel plates lubricated with the oleo-dispersions formulated with both smooth and porous fibers, i.e., obtained with DMAc:Ac and DM:Ac binary solvents, respectively, at different thickener content (3–5 wt.%). In these SEM micrographs, micropits, and grooves accompanied by plastic deformation on the worn surfaces can be distinguished, to different extent depending on the type and concentration of nanofibers. The size of wear scars slightly decreases with the thickener content in the oleo-dispersion (see average values in Table 3), especially in the case of smooth fibers, which means that nanofibers contribute to the formation of the protective film. More interestingly, the surfaces of the steel plates lubricated by oleo-dispersions produced with the porous fibers (Figure 9d–f) show wider wear marks under the same conditions. These results corroborates again that the oleo-dispersions formulated with smooth fibers are able to more easily release the oil entrapped in the 3D network, facilitating a steady oil replenishment in the contact, rather than the dispersions prepared with porous fibers, and are consistent with the oil loss results. Finally, as can be seen in Table 3, wear scar diameters obtained with smooth fibers are significantly lower than those achieved with the lithium grease and the CAb-free castor oil.

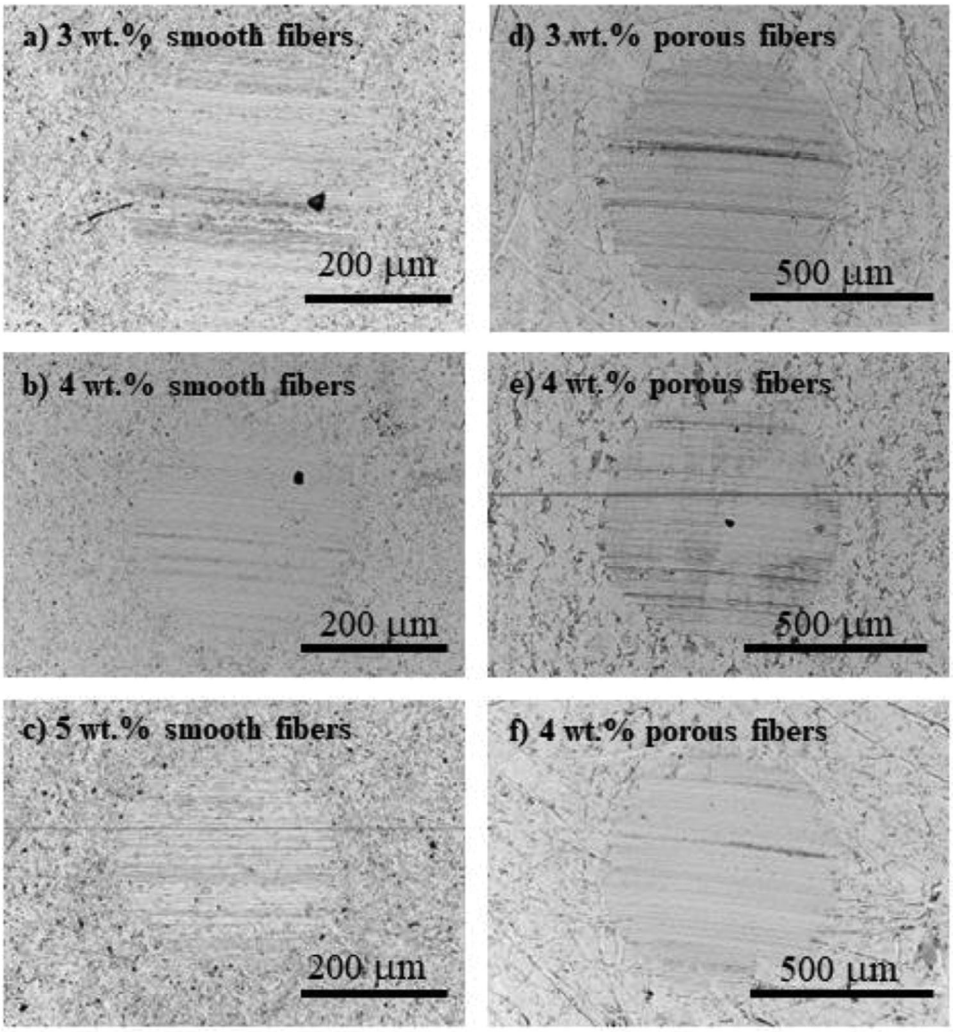

Figure 9. SEM micrographs of the worn plate surface in the steel/steel contacts lubricated with the oleo-dispersions of a–c) smooth and d–f) porous fibers, obtained with DMAc:Ac and DM:Ac binary solvents (15 wt.% spinning solution concentration), respectively, at different thickener concentration (3–5 wt.%).

3. Conclusion

In this research, cellulose acetate butyrate (CAb) nanostructures were successfully produced by electrospinning and validated as castor oil structuring agents for lubricant purposes. The spinnability of CAb solutions foreseen from experimental shear and extensional rheology and surface tension data correlates well with the production of uniform fibers. Bead-free uniform nanofibers were produced from CAb solutions that exhibit shear thinning behavior and a minimum relaxation time of ≈50 ms. These requisites were achieved for CAb concentrations above 10 wt.%, which corresponded to 2–2.5 times the entanglement concentration, C_e. In contrast, particles and BOAS morphologies were obtained from solutions with concentrations lower than C_e and slightly higher than C_e in the semidilute entangled regime, respectively. The increase of polymeric chain entanglements and decrease of surface tension were the key factors for improving the electrospinnability of CAb solutions.

Moreover, the morphology and texture of the electrospun nanostructures are highly dependent on the solvent selected, in particular its volatility. Certainly, one limitation of the electrospinning technique is the difficulty in finding green and appropriate solvents for cellulosic polymers. In this respect, there is still much room for improvement in the search for environmentally friendly solvents, where alternatives such as ionic liquids and NADES could be explored. However, a strong point of this technology is that the solvent can almost entirely be recovered in the electrospinning chamber by condensation.

Physically stable oleo-dispersions were obtained from electrospun CAb micro-/nano-structures and castor oil. The morphology and surface properties (i.e., smooth and porous textures) of the micro-/nano-structures and their concentration strongly impact the rheological and tribological properties of oleo-dispersions and serve to modulate them. Porous fibers and higher nanofiber concentrations impart higher thickening properties, which is attributed to larger fiber/oil interactions, also

resulting in higher oil retention ability. However, these porous nanostructures give rise to a less cohesive network, leading to a decrease in tackiness.

In general, the dispersions of CAb nanostructures in castor oil employed as lubricants in a tribological contact perform adequately, reducing friction and providing wear protection similar to, or even better than, a commercial lithium lubricating grease. Further, tribological measurements revealed that CAb smooth nanofibers instead of porous fibers as thickener enhance the friction-reducing and anti-wear properties of oleo-dispersions, which is attributed to a better release of the oil entrapped in the 3D network, thus facilitating a steady oil replenishment into the steel−steel contact.

In short, the oil structuring ability of these electrospun CAb nanoarchitectures opens up new opportunities in the lubricant industry to engineer innovative and bio-based functional thickening agents or additives toward the development of fully renewable lubricants.

4. Experimental Section

Materials: Commercial CAb with a number average molecular weight of 65.000 g mol^{-1} estimated by GPC, and DS_{acetyl} = 28−31 wt.%, $DS_{butyryl}$ = 16.5−19 wt.%, and $DS_{hydroxyl}$ = 0.8−1.40 wt.%, supplied by Merck Sigma-Aldrich, was used as spinning polymer. DMAc (purity ≥99.8%), DM (purity ≥99.8%), and Ac (purity ≥99.7%) supplied also by Merck Sigma-Aldrich were used as received for the preparation of CAb solutions. Castor oil purchased to Guinama (Spain) was used as biodegradable lubricating oil. A commercial multipurpose lithium lubricating grease (NLGI grade 2) commercialized by Bellota (Spain) was used as reference semisolid lubricant.

Preparation and Characterization of CAb Solutions: CAb solutions were prepared by dissolving CAb in a 1:2 (wt./wt.) DMAc:Ac binary solvent system to obtain solutions with concentrations ranging from 1.5 to 20 wt.%. This binary solvent was selected according to its high solving power for CAb, being appropriate for electrospinning.[31] Moreover, DMAc is low volatile and considered inherently biodegradable.[66] For the preparation of all solutions, the solvents were added to a pre-weighted amount of CAb in a glass flask and were magnetically stirred for 3 h at room temperature (≈23 °C). The intrinsic viscosity, [η], estimated from the viscosity of solutions and solvent by means of the Huggins and Kraemer treatments, of CAb in 1:2 (wt./wt.) DMAc:Ac was 201 mL g^{-1}. In addition, CAb was also dissolved in a 1:1 (wt./wt.) DM:Ac binary solvent system ([η] = 188 mL g^{-1}), at concentrations in the range 2.5–15 wt.%, following the same procedure, aiming to obtain different surface properties and morphologies in the CAb nanostructures. Despite being a volatile toxic solvent, DM was selected precisely because of its rapid evaporation during electrospinning and its capacity to create porous nanostructures.[67]

CAb solutions were physico-chemically characterized through electrical conductivity, surface tension, and shear and extensional viscosity measurements. Electrical conductivity of the polymer solutions was determined at 23 °C using a conductivity meter (GLP 31, Crison, Spain) and a dip-type cell (cell constant: 1.0 cm^{-1}; accuracy ± 0.5%), calibrated with standard KCl solutions in the appropriate concentration range. Surface tension was measured at 23 °C with a surface tensiometer (Sigma 703D, Biolin Scientific, China) using a platinum Wilhelmy plate. At least three measurements of electrical conductivity and surface tension were taken for each solution.

The shear viscosity of CAb solutions was measured by applying a stepped shear rate ramp in the range of 1–500 s^{-1}, also at 23 °C, using a controlled-strain rheometer (ARES Rheometric Scientific, UK) equipped with coaxial cylinders (32 mm inner diameter, 1 mm gap, 33.35 mm length). CAb solutions with higher concentrations exhibited a non-Newtonian response, and the shear rate dependence of viscosity was fitted to the Carreau–Yasuda model (R^2 < 0.995):

$$\eta = \eta_\infty + \frac{(\eta_0 - \eta_\infty)}{\left[1 + \left(\frac{\dot{\gamma}}{\dot{\gamma}_c}\right)^p\right]^{\frac{1-n}{p}}} \quad (3)$$

where, η is the non-Newtonian viscosity, η_∞ and η_0 are the high- and zero-shear rate limiting viscosities, respectively, $\dot{\gamma}$ is the shear rate, $\dot{\gamma}_c$ is the critical shear rate for the onset of the shear-thinning region, p is dimensionless constant, and n is the flow index which are related to the slope of the power-law viscosity decay. In addition, the extensional flow behavior of CAb solutions was measured at 23 °C by using a capillary break-up extensional rheometer (CaBER Haake, Thermo Scientific, Germany) with two 6 mm-diameter plates separated by an initial gap of 2 mm. A fluid drop was placed between the two plates and then stretched as the upper plate rapidly moved upward, thus creating a filament flowing under the viscous, elastic, and capillary forces. The diameter change of the filament mid-point was measured by using a laser micrometer which has the resolution of ≈5 µm and enables high-speed measurements. Having the change in filament diameter as a function of time, apparent extensional viscosity (η_{ext}) can be calculated according to the following equation:[37]

$$\eta_{ext} = -\frac{\sigma}{\frac{dD(t)}{dt}} \quad (4)$$

where σ is the surface tension of the fluid.

Electrospinning of CAb Solutions and Characterization of Electrospun Nanostructures: The CAb solutions were electrospun using a 18-gauge blunt needle at a flow rate of 0.6-1 mL h^{-1} fixed horizontally on a syringe pump in a commercial spinner (Startup, Doxa Microfluidics, Spain). A 13–15 kV voltage and 10 cm distance between the needle and the collector plate were applied for all samples. Random nanostructures were deposited on a stationary collector, which was covered by an aluminum foil. Electrospinning environmental conditions were maintained at ≈23 ± 1 °C and 45–55% relative humidity. Relative humidity was controlled via a small humidifier placed inside the enclosure. The morphology of the CAb nanostructures was examined in a FlexSEM 1000 II microscope (Hitachi, Japan). Samples were coated with a thin layer of gold prior to SEM imaging. The average fiber diameter was determined by choosing 100 randomly selected fibers using the ImageJ software.

Preparation of Oleo-Dispersion Formulations: CAb oleo-dispersions were prepared by blending selected electrospun CAb nanostructures and castor oil in an open batch reactor using an IKA RW-20 mixer device (Germany) equipped with an anchor impeller geometry. Samples were mixed for 30 min, at room temperature (≈23 °C) and rotational speed of 60 rpm. CAb contents in the blends were 3, 4, and 5 wt.%. After processing, all the samples were stored at least 24 h prior to perform further characterization.

Characterization of CAph Oleo-Dispersions—Rheological Measurements: The rheological tests were performed using a controlled-stress rheometer (Mars, Thermo Haake, Germany) with roughened stainless-steel parallel plates geometries (20 and 35 mm, 1 mm gap). A roughened surface was selected on account of the risk that the oleo-dispersions were prone to slip effects, and the diameter was selected on the basis of the different consistency exhibited by samples. All the samples were left to rest for 30 min before each measurement in order to eliminate residual stress history.

The viscoelastic response of oleo-dispersions was analyzed by means of small-amplitude oscillatory shear (SAOS) tests. First, stress sweep tests were completed at 1 Hz to determine the stress values within the linear viscoelastic region (LVR). Afterward, frequency sweep tests in the range 0.03–100 rad s^{-1} at 23 °C was subsequently performed by applying a stress within the linear viscoelastic regime. Further, the stickiness of the oleo-dispersions was investigated through probe tack tests. The dispersions were placed between the 35 mm parallel plate–plate geometry with a fixed gap of 0.3 mm and then a debonding speed of 1 mm s^{-1} was applied while recording the stress values. The contact between plate and dispersion was

maintained for 20 min before debonding to allow stress relaxation of samples.

Characterization of CAph Oleo-Dispersions—Oil Loss Measurements: The oil retention capacity of the oleo-dispersions was evaluated by measuring the weight of released oil after centrifugation. Two grams of oleo-dispersion was weighed in a centrifuge tube (45 mL), and then centrifuged for 10 min at 750 rpm. After that, oil loss was quantified by measuring the weight of remaining oleo-dispersion as follow:

$$\text{Oil loss } (\%) = \frac{W_1 - W_2}{W_1} \times 100 \quad (5)$$

where W_1, is the mass of oleo-dispersion and, W_2 is the mass of the dispersion after removing the part of separated oil after centrifugation.

Characterization of CAph Oleo-Dispersions—Penetration Tests: Penetration indexes and NLGI grades of selected samples were determined according to the ASTM D 1403 standard using a one-quarter cone geometry (Stanhope-Seta, UK). The one-quarter scale penetration values were converted into the equivalent full scale cone penetration values, following the ASTM D 217 standard.

Characterization of CAph Oleo-Dispersions—Dropping Point: The dropping point of selected samples was determined according to the ASTM D-2265 method.

Characterization of CAph Oleo-Dispersions—Tribological Measurements: Tribological tests were performed in a tribological cell coupled with a controlled-stress rheometer (Physica MCR-501, Anton Paar, Austria). The tribological cell was furnished with a 1/2 in. diameter steel ball (1.4401 Grade 100 AISI 316, roughness = 0.10 µm, Rockwell B-scale hardness = 79 HRB) rotating on three 45° inclined steel plates (1.4301 AISI 304, roughness = 0.21 µm, Rockwell B-scale hardness = 80 HRB). The evolution of the friction coefficient with the rotational speed was assessed in a range of sliding velocities between 10^{-4} and 10^{2} (m s^{-1}), at 23 °C, by applying 40 N normal load. The stationary friction coefficient was also obtained by applying a 40 N normal force and setting a constant sliding velocity (0.047 m s^{-1}) during 20 min. This test was repeated at least three times to obtain an accurate average friction coefficient value. Each test was performed with fresh ball-and-plate contact areas; also, all specimens were cleaned with ethanol. The wear marks left in the plates were observed in the FlexSEM 1000 II microscope (Hitachi, Japan) using a 15 kV extraction voltage.

Acknowledgements

This work is part of different research projects funded by MCIN/AEI/10.13039/501100011033 and by "ERDF A way of making Europe" (grant PID2021-125637OB-I00) and by FEDER/Junta de Andalucía Programmes (grants PY20_00751 and UHU202029). J.F.R.-V. has also received a Ph.D. Research Grant PRE2019-090632 from Ministerio de Ciencia e Innovación (Spain). Funding for open access charge: Universidad de Huelva/CBUA. Authors gratefully acknowledge the financial support.

Conflict of Interest

The authors declare no conflict of interest.

Author Contributions

All authors contributed to the study conception and design. M.A.M.A. and J.F.R.V. did experimental work and prepared Figures and Tables. J.E.M.A. supervised experimental work, wrote original manuscript, and reviewed final manuscript and Figures. J.M.F. supervised experimental work and wrote the original manuscript and the final version. All authors read and approved the final manuscript.

Data Availability Statement

The data that support the findings of this study are available from the authors upon reasonable request.

Keywords

cellulose acetate butyrate, electrospinning, nanofibers, rheology, sustainable lubricants

Received: November 22, 2023
Revised: January 12, 2024
Published online:

[1] B. T. Seymour, R. A. E. Wright, A. C. Parrott, H. Gao, A. Martini, J. Qu, S. Dai, B. Zhao, *ACS Appl. Mater. Interfaces* **2017**, *9*, 25038.
[2] L. R. Rudnick, *Synthetics, Mineral Oils, and Bio-Based Lubricants: Chemistry and Technology 3rd Ed.*, CRC Press, **2020**.
[3] J. Luo, X. Zhou, *Friction* **2020**, *8*, 643.
[4] K. Holmberg, A. Erdemir, *Tribol. Int.* **2019**, *135*, 389.
[5] S. Khan, P. Das, M. A. Quadir, M. Thaher, S. N. Annamalai, C. Mahata, A. H. Hawari, H. Al Jabri, *Sci. Total Environ.* **2022**, *847*, 157648.
[6] J. K. Mannekote, S. V. Kailas, K. Venkatesh, N. Kathyayini, *Renew. Sustain. Energy Rev.* **2018**, *81*, 1787.
[7] A. Abass O, A. T. Jameel, S. A. Muyubi, M. I. Abdul Karim, A. M. Z. Alam, *IIUM Eng. J.* **2011**, *12*, 161.
[8] L. A. Gil-Alana, M. Monge, *Resour. Policy* **2019**, *60*, 198.
[9] B. Soltannia, L. Martin-Alarcon, J. Uhryn, A. Govedarica, P. Egberts, M. Trifkovic, *J. Colloid Interface Sci.* **2023**, *645*, 560.
[10] P. Shetty, L. Mu, Y. Shi, *Carbohydr. Polym.* **2020**, *230*, 115670.
[11] T. Xia, Y. Huang, P. Lan, L. Lan, N. Lin, *Biomacromolecules* **2019**, *20*, 4457.
[12] J. E. Martín-Alfonso, M. J. Martín-Alfonso, C. Valencia, M. T. Cuberes, *Friction* **2021**, *9*, 415.
[13] J. E. Martín-Alfonso, M. J. Martín-Alfonso, J. M. Franco, *Appl. Clay Sci.* **2020**, *192*, 105632.
[14] R. Sánchez, G. B. Stringari, J. M. Franco, C. Valencia, C. Gallegos, *Carbohydr. Polym.* **2011**, *85*, 705.
[15] J. E. Martín-Alfonso, F. López-Beltrán, C. Valencia, J. M. Franco, *Tribol. Int.* **2018**, *123*, 329.
[16] M. Trejo-Cáceres, M. C. Sánchez, J. E. Martín-Alfonso, *Int. J. Biol. Macromol.* **2023**, *227*, 673.
[17] S. O. Ilyin, S. N. Gorbacheva, A. Y. Yadykova, *Tribol. Int.* **2023**, *178*, 108080.
[18] S. N. Gorbacheva, Y. M. Yarmush, S. O. Ilyin, *Tribol. Int.* **2020**, *148*, 106318.
[19] S. N. Gorbacheva, A. Y. Yadykova, S. O. Ilyin, *Cellulose* **2021**, *28*, 10203.
[20] M. Borrego, J. E. Martín-Alfonso, M. C. Sánchez, C. Valencia, J. M. Franco, *Int. J. Biol. Macromol.* **2021**, *180*, 212.
[21] J. F. Rubio-Valle, M. C. Sánchez, C. Valencia, J. E. Martín-Alfonso, J. M. Franco, *Ind. Crops Prod.* **2022**, *188*, 115579.
[22] J. F. Rubio-Valle, C. Valencia, M. Sánchez, J. E. Martín-Alfonso, J. M. Franco, *Cellulose* **2023**, *30*, 1553.
[23] S. N. Gorbacheva, A. Y. Yadykova, S. O. Ilyin, *Carbohydr. Polym.* **2021**, *272*, 118509.
[24] N. V. Reddy, B. S. Rao, V. V. R. N. Rao, *Mater. Lett.* **1992**, *13*, 147.
[25] N. R. Saha, I. Roy, G. Sarkar, A. Bhattacharyya, R. Das, D. Rana, R. Banerjee, A. K. Paul, R. Mishra, D. Chattopadhyay, *Carbohydr. Polym.* **2018**, *187*, 8.
[26] L. S. Blachechen, J. P. de Mesquita, E. L. de Paula, F. V. Pereira, D. F. S. Petri, *Cellulose* **2013**, *20*, 1329.

[27] H.-L. Tan, D. Kai, P. Pasbakhsh, S.-Y. Teow, Y.-Y. Lim, J. Pushpamalar, *Colloids Surfaces B Biointerfaces* **2020**, *188*, 110713.
[28] A. Tanvir, V. P. Ting, S. J. Eichhorn, *Mater. Lett.* **2020**, *261*, 127116.
[29] P. Pascariu, L. Olaru, A. L. Matricala, N. Olaru, *Appl. Surf. Sci.* **2018**, *455*, 61.
[30] S. A. Hosseini, M. Soltanieh, S. M. Mousavi, *Desalin. WATER Treat.* **2017**, *64*, 127.
[31] C. Huang, Y. Tang, X. Liu, A. Sutti, Q. Ke, X. Mo, X. Wang, Y. Morsi, T. Lin, *Soft Matter* **2011**, *7*, 10812.
[32] Y. Liu, G. Ma, D. Fang, J. Xu, H. Zhang, J. Nie, *Carbohydr. Polym.* **2011**, *83*, 1011.
[33] L. Van der Schueren, I. Steyaert, B. De Schoenmaker, K. De Clerck, *Carbohydr. Polym.* **2012**, *88*, 1221.
[34] R. Rošic, J. Pelipenko, P. Kocbek, S. Baumgartner, M. Bešter-Rogač, J. Kristl, *Eur. Polym. J.* **2012**, *48*, 1374.
[35] S. Formenti, R. Castagna, R. Momentè, C. Bertarelli, F. Briatico-Vangosa, *Eur. Polym. J.* **2016**, *75*, 46.
[36] D. Fang, Y. Liu, S. Jiang, J. Nie, G. Ma, *Carbohydr. Polym.* **2011**, *85*, 276.
[37] G. H. McKinley, A. Tripathi, *J. Rheol.* **2000**, *44*, 653.
[38] Q. Zhang, J. Lin, Y. Dong, F. Sun, *Colloids Surfaces A Physicochem. Eng. Asp.* **2023**, *661*, 130950.
[39] C. L. Berli, J. . Deiber, M. Añón, *Food Hydrocoll* **1999**, *13*, 507.
[40] M. G. McKee, G. L. Wilkes, R. H. Colby, T. E. Long, *Macromolecules* **2004**, *37*, 1760.
[41] R. H. Colby, *Rheol. Acta* **2010**, *49*, 425.
[42] W. Graessley, *Polymer* **1980**, *21*, 258.
[43] S. L. Shenoy, W. D. Bates, H. L. Frisch, G. E. Wnek, *Polymer* **2005**, *46*, 3372.
[44] R. R. Klossner, H. A. Queen, A. J. Coughlin, W. E. Krause, *Biomacromolecules* **2008**, *9*, 2947.
[45] S. Morozova, P. W. Schmidt, A. Metaxas, F. S. Bates, T. P. Lodge, C. S. Dutcher, *ACS Macro Lett.* **2018**, *7*, 347.
[46] L. Campo-Deaño, C. Clasen, *J. Nonnewton. Fluid Mech.* **2010**, *165*, 1688.
[47] O. Akhlaghi, O. Akbulut, Y. Z. Menceloglu, *Eur. Polym. J.* **2015**, *73*, 17.
[48] E. Miller, C. Clasen, J. P. Rothstein, *Rheol. Acta* **2009**, *48*, 625.
[49] S. Różańska, K. Verbeke, J. Różański, C. Clasen, P. Wagner, *J. Polym. Sci. Part B Polym. Phys.* **2019**, *57*, 1537.
[50] M. R. Duxenneuner, P. Fischer, E. J. Windhab, J. J. Cooper-White, *Biomacromolecules* **2008**, *9*, 2989.
[51] M. Srinivasarao, D. Collings, A. Philips, S. Patel, *Science* **2001**, *292*, 79.
[52] A. Altan, Z. Aytac, T. Uyar, *Food Hydrocoll* **2018**, *81*, 48.
[53] H. Fong, I. Chun, D. Reneker, *Polymer* **1999**, *40*, 4585.
[54] L. Palangetic, N. K. Reddy, S. Srinivasan, R. E. Cohen, G. H. McKinley, C. Clasen, *Polymer* **2014**, *55*, 4920.
[55] J. H. Yu, S. V. Fridrikh, G. C. Rutledge, *Polymer* **2006**, *47*, 4789.
[56] K. Almdal, J. Dyre, S. Hvidt, O. Kramer, *Polym. Gels Networks* **1993**, *1*, 5.
[57] J. D. Ferry, *Viscoelastic properties of polymers*, **1980**.
[58] J. E. Martín-Alfonso, C. Valencia, M. C. Sánchez, J. M. Franco, C. Gallegos, *Eur. Polym. J.* **2007**, *43*, 139.
[59] M. Harmon, B. Powell, I. Barlebo-Larsen, R. Lewis, *Tribol. Trans.* **2019**, *62*, 207.
[60] B. Çavdar, K. C. Ludema, *Wear* **1991**, *148*, 347.
[61] M. A. Martín-Alfonso, J. F. Rubio-Valle, J. P. Hinestroza, J. E. Martín-Alfonso, *Gels* **2022**, *8*, 504.
[62] D. Gonçalves, S. Pinho, B. Graça, A. V. Campos, J. H. O. Seabra, *Tribol. Int.* **2016**, *96*, 87.
[63] D. Gonçalves, B. Graça, A. V. Campos, J. Seabra, *Tribol. Int.* **2016**, *93*, 399.
[64] E. Cortés-Triviño, C. Valencia, M. A. Delgado, J. M. Franco, *J. Ind. Eng. Chem.* **2019**, *80*, 626.
[65] M. A. Delgado, E. Cortés-Triviño, C. Valencia, J. M. Franco, *Tribol. Int.* **2020**, *146*, 106231.
[66] X. Chen, C. Yang, W. Wang, B. Ge, J. Zhang, Y. Liu, Y. Nan, *J. Environ. Sci.* **2017**, *53*, 88.
[67] A. Celebioglu, T. Uyar, *Mater. Lett.* **2011**, *65*, 2291.